Design and Analysis of Vertical-Cavity Semiconductor Optical Amplifiers

Joachim Piprek, *Senior Member, IEEE*, Staffan Björlin, and John E. Bowers, *Fellow, IEEE*

Abstract—The authors present detailed, yet largely analytical, models for gain, optical bandwidth, and saturation power of vertical-cavity semiconductor optical amplifiers (VCSOAs) in reflection and transmission mode. Simple formulas for the gain-bandwidth product are derived. The saturation model considers a sublinear material gain, gain enhancement by the standing-wave effect, and all relevant carrier recombination mechanisms. Excellent agreement with measurements on novel 1.3-μm VCSOAs is obtained. The models are used to analyze device performance and to investigate optimization options. Parameter plots are given which allow for an easy exploration of the VCSOA design space, matching desired performance data with the required mirror reflectivity and pump current.

Index Terms—Fabry–Perot resonators, nonlinear equations, optical fiber devices, optical filters, optical resonators, optical saturation, quantum-well devices, semiconductor device modeling, semiconductor optical amplifiers, surface-emitting lasers.

I. INTRODUCTION

R ECENTLY, vertical-cavity semiconductor optical amplifiers (VCSOAs) have been the topic of increasing interest. They are potential low-cost alternatives to in-plane SOAs and they have the inherent advantage of polarization insensitivity, high-fiber coupling efficiency, and low noise figure. Two-dimensional arrays of VCSOAs are attractive for parallel applications. Several groups have fabricated VCSOAs based on GaAs (0.97-μm wavelength) [1] or InP (1.55 μm) [2], [3]. We have recently demonstrated the first 1.3-μm vertical-cavity amplifiers [4]. VCSOAs operating at a 1.3-μm wavelength are desirable fiber optic components. Commercial 1.3-μm vertical-cavity surface-emitting lasers (VCSELs) are already in production [5]. Those optically pumped VCSELs use GaAs/InP wafer fusion to combine InP-based gain regions with highly reflective AlGaAs/GaAs mirrors.

The refractive index profile in the center part of our double-fused, planar, and undoped vertical-cavity amplifier is shown in Fig. 1. Two 1.3-μm AlAs/GaAs distributed Bragg reflectors (DBRs) with 25 (bottom) and 13 (top) periods, respectively, are fused to an InP-based active region. The DBR spacing is about 1 μm, 2.5 times the internal signal wavelength. The active region contains three stacks of seven compressively strained 6.3-nm thick InAs$_{0.5}$P$_{0.5}$ quantum-wells (QWs) and strain-compensating In$_{0.8}$Ga$_{0.2}$P barriers. The three multi-quantum-well (MQW) stacks are placed at the three central peaks of the standing optical wave (Fig. 1). The 21 quantum wells are designed to have maximum optical gain at the signal wavelength (Fig. 2). The quantum wells are also the only layers in our structure to allow for band-to-band absorption of the 980-nm pump laser beam. The pump beam is focused through the bottom GaAs substrate to a small spot of about 8 μm in diameter. The input signal is generated by a tunable 1.3-μm laser and it is coupled in and out through the front DBR using a circulator (signal spot size 4 μm). Focusing and matching both the light beams is crucial to achieve sufficient optical gain in our planar device. A 1.3-μm anti-reflection coating was applied to the GaAs substrate to avoid interference from backside signal reflection. The output signal is monitored by an optical spectrum analyzer. With 13 front mirror periods, the best performance parameters measured at different pump levels are 9.4-dB fiber-to-fiber gain, 90-GHz optical bandwidth (0.5 nm), and −6.1-dBm saturation output power. At different signal wavelengths, other VCSOAs have already shown higher gain [1], [2] and larger bandwidth [3].

To improve the performance of present VCSOAs, a more detailed understanding of design options is highly desirable. The design theory for Fabry–Perot in-plane SOAs is well developed (see, e.g., [6]); however, some limiting factors are often neglected, like the sublinear increase of the material gain with rising carrier density (see inset of Fig. 2). Moreover, vertical-cavity devices exhibit important differences. The short vertical cavity allows for only one longitudinal mode. Thin active layers are passed in the vertical direction and the single-pass gain is very small. However, the material gain may be enhanced by up to a factor two if the active layers are placed at the peaks of the standing optical waves. Highly reflective DBRs are required for reasonable amplifier gain. Light penetration into these mirrors substantially enlarges the effective cavity length (Fig. 1) which needs to be considered in Fabry–Perot-type models. There are very few publications on the design theory of VCSOAs [7], [8]. Those papers neglect essential properties of vertical-cavity amplifiers and do not validate their calculations by measurements.

In the following, we derive a detailed yet largely analytical one-dimensional VCSOA model both for operation in reflection mode (signal output through top DBR) and transmission mode (signal output through bottom DBR). The model for gain and bandwidth is based on the Fabry–Perot resonator approach and the saturation model uses single mode rate equations. Measured characteristics from [9] are employed for validation as well as for the extraction of internal device parameters. We will show that design optimization can lead to major performance improvements.
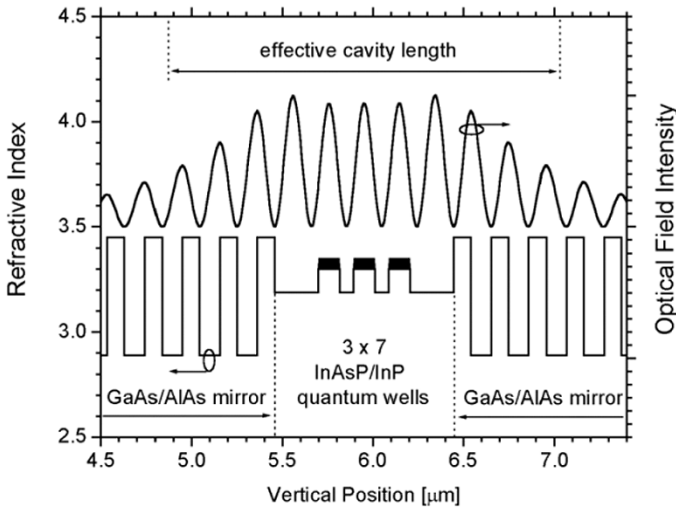
Fig. 1.   Refractive index profile and standing optical wave in the center of our double-fused 1.3-μm vertical-cavity amplifier.
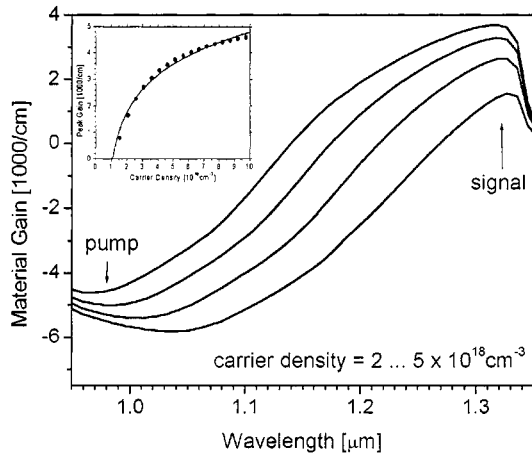

Fig. 2.   Calculated quantum well gain spectra at four different carrier densities. The inset gives the peak gain versus carrier density (dots) including the fit by (8) (line).

II. THEORY AND DESIGN RULES

A. Gain and Bandwidth

A common modeling approach to vertical cavity lasers is the replacement of the DBRs by hard mirrors of the same reflectivity which are separated by an effective cavity length L_c [10]. This way, we can start with the well-known gain formulas of Fabry–Perot amplifiers (G_R: reflection mode; G_T: transition mode) [7]

$$G_R = \frac{(\sqrt{R_f} - \sqrt{R_b}G_s)^2 + 4\sqrt{R_fR_b}G_s \sin^2 \Phi}{(1 - \sqrt{R_fR_b}G_s)^2 + 4\sqrt{R_fR_b}G_s \sin^2 \Phi} \quad (1)$$

$$G_T = \frac{(1 - R_f)(1 - R_b)G_s}{(1 - \sqrt{R_fR_b}G_s)^2 + 4\sqrt{R_fR_b}G_s \sin^2 \Phi} \quad (2)$$

with the front mirror reflectivity R_f, the back mirror reflectivity R_b, the single-pass gain G_s, and the single-pass phase detuning Φ. These equations allow for some general design considera-

tions. The maximum gain is achieved with $\Phi = 0$, when the signal wavelength is identical to the Fabry–Perot resonance. The amplifier needs to operate at $G_s^2 R_f R_b < 1$ to avoid lasing. Assuming typical DBR reflectivities, the lines in Fig. 3 represent the lasing threshold $G_s^2 R_f R_b = 1$ which gives the upper limit of the reflectivity design space as a function of the single-pass gain. Close approximation of this limit allows for high amplifier gain. Equation (1) leads to another rule for the reflection mode. The gain G_R drops below unity if $G_s^2 < R_b^{-1}$ since the emission through the back mirror exceeds the single-pass gain. These rules apply to all Fabry–Perot amplifiers, however VCSOAs exhibit much smaller values G_s and larger reflectivities than in-plane devices. For VCSOAs, the peak reflectivity of lossless DBRs with m periods ($2m$ layers) is given by [11]

$$R_{\text{DBR}} = \left(\frac{1 - qp^{2m-1}a}{1 + qp^{2m-1}a}\right)^2 \quad (3)$$

using the low-to-high refractive index ratios of the two DBR layers (p), as well as at the first (q) and the last (a) DBR interface. Assuming refractive indexes of 3.45 (GaAs) and 2.89 (AlAs), we calculate $R_f = 0.985$ and $R_b = 0.999$ for our device. Absorption or diffraction within the mirror reduces the reflectivity [12]. The wavelength dependence of the DBR reflectivity is ignored here since the reflection bandwidth of typical DBRs is much larger (about 100 nm in our case) than the amplifier bandwidth, and the cavity resonance wavelength λ_c is assumed identical to the DBR center wavelength. Our one-dimensional model also neglects the transversal optical mode structure. Resonance wavelengths differ slightly among transversal modes. The phase Φ in (1), (2) gives the deviation of the signal wavelength λ from λ_c

$$\Phi = 2\pi n_c L_c \left(\frac{1}{\lambda} - \frac{1}{\lambda_c}\right) \quad (4)$$

with the cavity refractive index n_c. The effective cavity length L_c is larger than the DBR distance L_m and it includes the phase penetration depths L_f and L_b into the front and back DBR, respectively, ($L_c = L_f + L_m + L_b$). The phase penetration depth L_p of a lossless DBR at the center wavelength λ_c is given by [13]

$$L_p = \frac{\lambda_c}{4n_c} \times \frac{q}{1-p} \times \frac{(1 - a^2p^{2m-1})(1 - p^{2m})}{1 - q^2a^2p^{4m-2}}. \quad (5)$$

With $n_c = 3.2$, the DBR penetration depth in our device is about 585 nm, resulting in the effective cavity length $L_c = 2.2$ μm (Fig. 1). Due to the high index contrast, AlAs/GaAs DBRs exhibit smaller penetration depths than mirrors grown on InP. The cavity refractive index n_c is obtained by averaging over all layers between the two DBRs. Typically, it is somewhat higher than the refractive index of the spacer material (InP) at the target wavelength; however, it can be affected by the quantum well carrier density as well as by device heating.

The remaining parameter in (1), (2) to be discussed is the single-pass signal gain G_s. Assuming laterally uniform mate-

rial properties across the signal spot, the single-pass gain in a VCSOA is calculated from the active region material gain g by

$$G_s = \exp[\xi g L_a - \alpha_c L_c] \qquad (6)$$

with the gain enhancement factor $\xi (\xi < 2)$, the total thickness L_a of all quantum wells, and the average cavity loss coefficient α_c. Gain enhancement results from the placement of the active region(s) at the peak(s) of the standing optical wave with [14]

$$\xi = 1 + \frac{\sin(2\pi n_c L_{\mathrm{MQW}}/\lambda_c)}{2\pi n_c L_{\mathrm{MQW}}/\lambda_c} \qquad (7)$$

(L_{MQW}—thickness of each MQW stack). We calculate $\xi = 1.75$ for our periodic gain structure (Fig. 1). Equation (6) can also be written in the more general form $G_s = \exp[g_m L_c]$ with the net modal gain $g_m = \xi \Gamma g - \alpha_c$ and the confinement factor $\Gamma = L_a/L_c$. However, calculation of the quantum well material gain g is the main challenge of VCSOA modeling. The optical gain depends on the QW carrier density N, the signal wavelength λ, the temperature T, and the photon density S. Assuming $\lambda = \lambda_c$, room temperature, and relatively low photon densities, the quantum well gain can be approximated by [10]

$$g(N) = g_o \ln\left(\frac{N + N_s}{N_{\mathrm{tr}} + N_s}\right) \qquad (8)$$

with the transparency carrier density N_{tr} and the fit parameters g_o and N_s. We calculate the optical gain of our strained MQWs utilizing an advanced laser simulation software [15]. The conduction bands are assumed to be parabolic and the non-parabolic valence bands are computed by the 4×4 **kp** method including valence band mixing [16]. The gain calculations employ a Lorentzian broadening function with 0.2-ps intraband relaxation time. The resulting gain spectra are shown in Fig. 2 for four different carrier densities. Strong absorption is calculated at the pump wavelength and the gain is maximum at the signal wavelength. The spectral width of the gain is on the order of 100 nm. The carrier density dependence at the signal wavelength 1.32 μm can be fitted by (8) using the parameters $g_o = 1580$ cm^{-1}, $N_{\mathrm{tr}} = 1.1 \times 10^{18}$ cm^{-3}, and $N_s = -0.63 \times 10^{18}$ cm^{-3} (inset of Fig. 2).

The VCSOA bandwidth is mainly restricted by the linewidth of the Fabry–Perot modes. From (1) and (2), one can easily obtain the following formulas for the amplifier bandwidth in reflection and transmission mode, respectively:

$$\Delta f_R = \frac{c}{\pi n_c L_c} \times \arcsin\{4\sqrt{R_f R_b}G_s[(1 - \sqrt{R_f R_b}G_s)^{-2}$$

$$- 2(\sqrt{R_f} - \sqrt{R_b}G_s)^{-2}]\}^{-1/2} \qquad (9)$$

$$\Delta f_T = \frac{c}{\pi n_c L_c} \times \arcsin\{(4\sqrt{R_f R_b}G_s)^{-1}$$

$$\times (1 - \sqrt{R_f R_b}G_s)^2\}^{1/2} \qquad (10)$$

(c: vacuum light velocity). These formulas give the full width at half maximum (-3 dB). In general, the bandwidth decreases
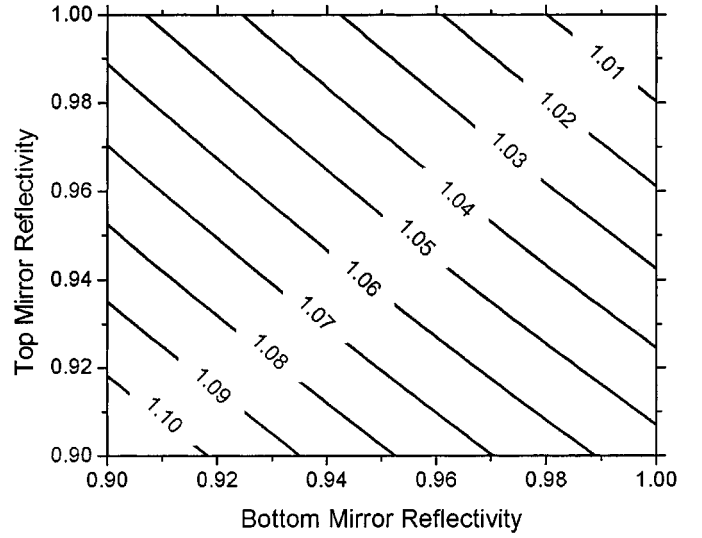

Fig. 3. Design limits of vertical-cavity amplifiers with the single-pass gain G_s as a parameter. The lines give the lasing threshold which imposes an upper limit on mirror reflectivity combinations.

as the peak gain increases. The square root of the peak gain times the bandwidth give a figure of merit that is practically constant (gain-bandwidth product). The threshold condition and the approximation $\sin(x) = x$ (for small x) leads to the simple formulas

$$\sqrt{G_R^0}\Delta f_R = \frac{c}{2\pi n_c L_c}\left(\frac{1}{\sqrt{R_f}} - \sqrt{R_f}\right) \qquad (11)$$

$$\sqrt{G_T^0}\Delta f_T = \frac{c}{2\pi n_c L_c}\sqrt{\frac{(1 - R_f)(1 - R_b)}{\sqrt{R_f R_b}}}. \qquad (12)$$

These equations are valid for any Fabry–Perot amplifier and their results are identical for symmetrical devices ($R_f = R_b$). In the reflection case, (11) is restricted to gain values well above 3 dB, since the initial reflection causes a singularity of (9). Remarkably, the gain-bandwidth product in reflection mode does not depend on the bottom reflectivity R_b and gain-bandwidth measurements can be used to verify the front reflectivity R_f or the optical cavity length $n_c L_c$.

B. Saturation Power

High-signal power results in gain saturation due to carrier depletion within the active layers. We use steady-state rate equations for carriers and photons to describe the saturation effect. In VCSOAs, only a single longitudinal mode needs to be considered. Equation (13) summarizes all physical mechanisms which affect the average carrier density N within the active layers. The first term describes external pumping by an effective current density j_p which is related to the optical pump power (e: electron charge). In Section III, we shall use j_p as a fit parameter, since our optical pump efficiency is hard to calculate. The carrier recombination rate $R(N) = AN + BN^2 + CN^3$ in (13) includes defect recombination (discussed below), spontaneous photon emission ($B = 10^{-10}$ cm^3/s), and Auger recombination ($C = 2 \times 10^{-29}$ cm^6/s)—material parameters are given for typical 1.3-μm InGaAsP active layers [17]. In linear approxima-

tion, the carrier lifetime τ_c is often employed as $R(N) = N/\tau_c$. However, in long-wavelength amplifiers, Auger recombination may cause significant deviations from the linear approximation. The last term in (13) gives the stimulated recombination rate (v_g: photon group velocity, and S: average photon density). The gain enhancement factor ξ accounts for the standing-wave effect. A linear gain approximation $g(N) = \gamma(N - N_{\mathrm{tr}})$ is often used which is appropriate for small carrier densities (cf. Fig. 2). We avoid linear approximations here to find more realistic performance predictions for strong pumping and large carrier densities

$$\frac{dN}{dt} = \frac{j_p}{eL_a} - (AN + BN^2 + CN^3) - \xi g(N)v_g S = 0 \tag{13}$$

$$\frac{dS}{dt} = (1 - R_f)\frac{\lambda_c}{hc}\frac{P_{\mathrm{in}}}{A_{\mathrm{in}}L_c} + \xi\Gamma g(N)v_g S + \beta\Gamma BN^2 - (\alpha_c + \alpha_m)v_g S = 0. \tag{14}$$

The second rate equation summarizes all physical mechanisms that affect the average photon density S [see (14)]. The first term describes the photon density increase resulting from the signal power P_{in} per area A_{in} entering through the front mirror (h—Planck's constant). The next two terms represent stimulated and spontaneous photon generation rates, respectively. The coefficient β gives the fraction of spontaneously emitted photons that is coupled into the signal mode. In our case, β is about 0.01 [10]. The last term in (14) represents all photon losses, including cavity absorption and scattering ($\alpha_c = 15$ cm^{-1}) as well as photon transmission trough the mirrors with

$$\alpha_m = \frac{1}{L_c}\ln\left[\frac{1}{\sqrt{R_f R_b}}\right]. \tag{15}$$

For our device, we calculate $\alpha_m = 36$ cm^{-1}. Equation (14) delivers the equilibrium photon density

$$S_o = \frac{1}{v_g}\left(\beta\Gamma BN^2 + \frac{\lambda_c(1 - R_f)P_{\mathrm{in}}}{hcA_{\mathrm{in}}L_c}\right)$$
$$\times (\alpha_m + \alpha_c - \xi\Gamma g(N))^{-1} \tag{16}$$

which becomes very large near lasing threshold. The threshold is defined by $\xi\Gamma g(N) = \alpha_m + \alpha_c$ which is equivalent to $R_f R_b G_s^2 = 1$. Alternatively, the average photon density S_o in amplifiers may be calculated from the Fabry–Perot approach [8], [18] which results in significantly larger numbers. Both methods are known to give different results [6] and we find full agreement with the measurements only by using the rate equation approach.

Introducing (16) into (13), an implicit equation for the equilibrium carrier density N_o is obtained which is rather difficult to solve. This situation can be simplified by looking at two specific steady-state cases which are of special interest with amplifiers. In the unsaturated case with small input power P_{in}, the photon density S_o is low and the stimulated recombination in (13) is negligibly small compared to $R(N)$. In other words, carrier density N_o, material gain $g(N_o)$, single-pass gain G_s as well as the amplifier gain (G_T, G_R) are independent on the input power which is desirable for typical amplifier operation. However, with increasing input power, the stimulated recombination rate rises and the carrier density eventually starts to decrease. This results in lower material gain and lower amplifier gain. The saturation input power $P_{\mathrm{in,sat}}$ is reached when the amplifier gain drops to half its maximum value. Signal input and output power at saturation are key performance parameters of amplifiers and they can be calculated analytically from above equations without any simplification, as shown in the following.

First, the unsaturated carrier density N_u is obtained from the weak signal equilibrium limit of (13) ($S = 0$) which gives a simple cubic equation having the solution

$$N_u = \left[\sqrt{\left(\frac{u}{3}\right)^3 + \left(\frac{w}{2}\right)^2} - \frac{w}{2}\right]^{\frac{1}{3}}$$
$$- \frac{u}{3}\left[\sqrt{\left(\frac{u}{3}\right)^3 + \left(\frac{w}{2}\right)^2} - \frac{w}{2}\right]^{-\frac{1}{3}} - \frac{B}{3C}$$
$$u = \frac{2}{27}\left(\frac{B}{C}\right)^3 - \frac{BA}{3C^2} - \frac{j_p}{eL_a C}, \quad w = \frac{A}{C} - \frac{1}{3}\left(\frac{B}{C}\right)^2. \tag{17}$$

Using (1) and (2), the carrier density N_u leads to the unsaturated peak gain G_{Ru} and G_{Tu}, respectively. The saturation carrier densities for reflection and transmission mode are then given by

$$N_{Rs} = (N_{\mathrm{tr}} + N_s)\exp\left[\frac{\alpha_c}{\xi\Gamma g_o}\right]$$
$$\times \left\{\frac{\sqrt{0.5 \times G_{Ru}} + \sqrt{R_f}}{\sqrt{R_f R_b}\sqrt{0.5 \times G_{Ru}} + \sqrt{R_b}}\right\}^{\frac{1}{\xi\Gamma g_o L_c}} - N_s \tag{18}$$

$$N_{Ts} = (N_{\mathrm{tr}} + N_s)\exp\left[\frac{\alpha_c}{\xi\Gamma g_o}\right]$$
$$\times \left\{r - \sqrt{r^2 - \frac{1}{R_f R_b}}\right\}^{\frac{1}{\xi\Gamma g_o L_c}} - N_s \tag{19}$$
$$r = \frac{G_{Tu}\sqrt{R_f R_b} + (1 - R_f)(1 - R_b)}{G_{Tu}R_f R_b}.$$

From these saturation carrier densities we obtain the saturation input power using (13) and (16)

$$P_{\mathrm{in,sat}}(N_{\mathrm{sat}}) = \frac{hcA_{\mathrm{in}}L_c}{\lambda_c(1 - R_f)}\left[\left(\frac{j_p}{eL_a} - R(N_{\mathrm{sat}})\right)\right.$$
$$\times \left.\left(\frac{\alpha_m + \alpha_c}{\xi g(N_{\mathrm{sat}})} - \Gamma\right) - \beta\Gamma BN_{\mathrm{sat}}^2\right] \tag{20}$$
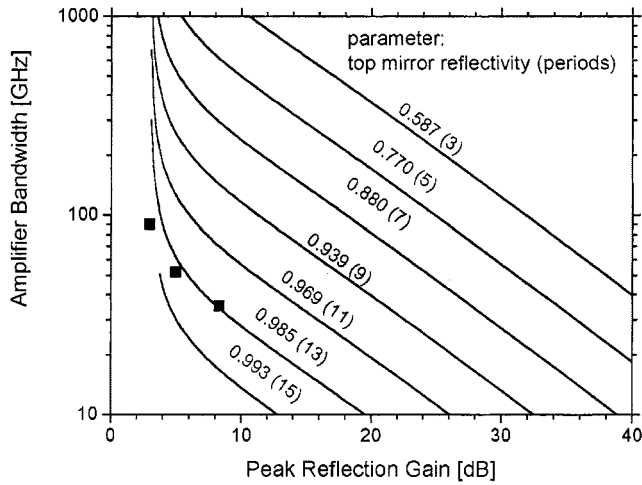
Fig. 4. Optical bandwidth versus peak gain in reflection mode. Dots give measured data. Lines are calculations by (9) for 25 bottom mirror periods with the top mirror reflectivity (periods) as parameter.
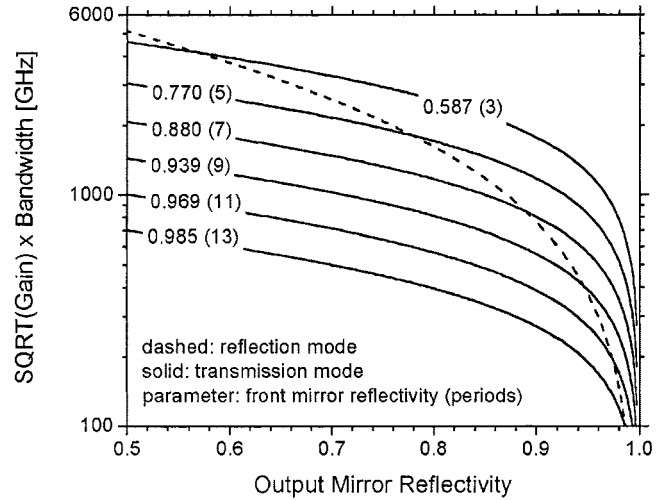

Fig. 5. Square-root (gain) times bandwidth versus output mirror reflectivity as calculated by (11) and (12) for reflection mode (dashed) and transmission mode (solid), respectively. For the transmission mode, the top mirror reflectivity (periods) is given as parameter.
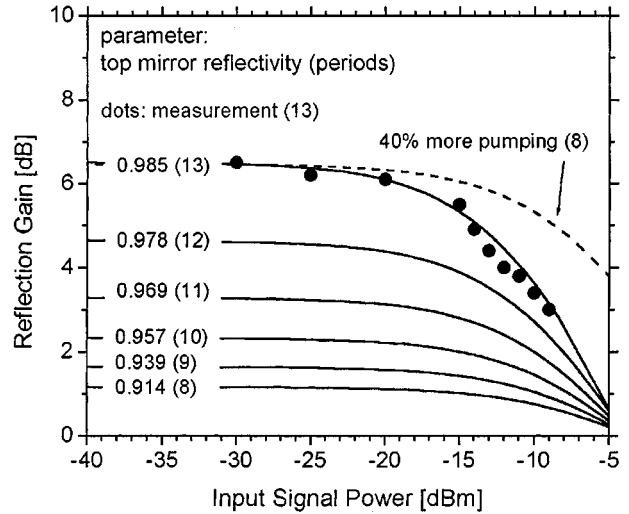

Fig. 6. Gain versus input signal power in reflection mode. Dots are measured with 150-mW pump power; solid lines represent numerical results for 25 bottom mirror periods and different top mirror reflectivities (periods). The dashed line is calculated for eight top mirror periods and 40% stronger pumping.

with $N_{\text{sat}} = N_{Rs}$ or $N_{\text{sat}} = N_{Ts}$ for reflection or transmission mode, respectively. The saturation output power for both modes is

$$P^R_{\text{out,sat}} = P_{\text{in,sat}}(N_{Ru})\frac{G_{Ru}}{2}$$

$$P^T_{\text{out,sat}} = P_{\text{in,sat}}(N_{Tu})\frac{G_{Tu}}{2}. \qquad (21)$$

III. PERFORMANCE ANALYSIS AND OPTIMIZATION

To validate the model and to specify internal parameters, we first simulate measured device characteristics. Fig. 4 shows measured bandwidth data in reflection mode versus peak gain. For comparison, calculated curves are plotted for different front mirror reflectivities. The lines are generated by varying the signal pass gain G_s from $R_b^{-0.5}$ to $(R_f R_b)^{-0.5}$ (threshold). Best agreement with the measurement is obtained for $R_f = 0.985$, exactly as expected for 13 top mirror GaAs/AlAs periods. The slight deviation is attributed to signal coupling losses. Due to the initial reflection, the bandwidth approaches infinity near 3-dB amplifier gain. Lower top mirror reflection allows for larger gain and/or larger bandwidth, however, higher single-pass gain is required. With our present 13 top mirror periods, 10-dB gain, and 30-GHz bandwidth are obtained with $G_s = 1.007$ which corresponds to $g = 440$ cm^{-1} quantum well gain and $N = 1.24 \times 10^{18}$ cm^{-3} carrier density. Thinning the top mirror to five periods, for example, 500-GHz bandwidth could be obtained for 10-dB gain, requiring $G_s = 1.07, g = 3100$ cm^{-1}, and $N = 3.83 \times 10^{18}$ cm^{-3}. For 30-GHz bandwidth, five mirror periods could give a 36-dB gain if an even higher value of $G_s = 1.135$ is achieved ($g = 5600$ cm^{-1}, $N = 16 \times 10^{18}$ cm^{-3}). The latter case seems out of reach but it helps to understand that extremely high pumping levels may be required along those design curves.

The calculated gain-bandwidth product as a function of the output mirror reflectivity is plotted in Fig. 5 for reflection and transmission mode. Lower reflectivity gives higher bandwidth in both cases. The reflection mode curve (dashed) crosses transmission mode curves (solid) for symmetric devices ($R_f = R_b$).

This leads to the intuitive result that the transmission mode gives a higher gain-bandwidth product than the reflection mode if $R_b < R_f$ (and vice versa).

The dots in Fig. 6 represent measured data for the reflection gain as a function of input power. To simulate this curve, the steady-state carrier rate equation is solved numerically using the average photon density given by (16). Several internal parameters are involved in this simulation which are not exactly known. We consider both the effective pump current density j_p and the defect recombination parameter A as most critical and vary both numbers to find agreement with the measurement in Fig. 6. The fit gives $j_p = 540$ A/cm^2 and the defect recombination lifetime $A^{-1} = 15$ ns which is a measure of active region growth quality. With low input power, we extract 1.18×10^{18} cm^{-3} average QW carrier density and 5-ns carrier lifetime. However, the pumping efficiency seems to be quite low, the effective injection current

per quantum well is only 26 A/cm^2 leaving room for substantial improvement. From the calculated QW absorption coefficient $\alpha_{qw} = 5000$/cm at $\lambda_p = 980$ nm (Fig. 2), we estimate about 30 times higher pump current densities

$$j_p = eL_a \frac{T_p P_p}{A_p} \times \frac{\lambda_p}{hc} \times \frac{1 - \exp(-\alpha_{\mathrm{qw}} L_a)}{L_a} \qquad (22)$$

assuming a pump beam transmittance of $T_p \sim 1$ (pump power $P_p = 150$ mW, pump area $A_p = 50$ μm^2). The poor pumping efficiency is attributed to optical losses as well as to lateral carrier spreading which is not yet included in our model. The pump area is about four times larger than the signal spot. Better matching and higher pump power are expected to allow for significant performance improvements. Fig. 6 also predicts the performance with lower top mirror reflectivity. The input saturation power increases as the number of top mirror periods decreases. The decay in reflection gain can easily be compensated for by stronger pumping (dashed line).

Based on (21), the relation between peak gain and output saturation power is shown in Fig. 7 for a wide range of output DBR periods. The lines are generated by varying the pump current, starting at the transparency current on the left and ending at the lasing threshold on the right. Thus, the QW carrier density is continuously increased along the lines. The peak gain refers to the unsaturated carrier density N_u whereas the saturation power is calculated from the somewhat smaller carrier density N_{sat} at saturation. With small gain ($N_u > N_{\mathrm{tr}}$), the saturation power peaks sharply at $N_{\mathrm{sat}} = N_{\mathrm{tr}}$ since the material gain is zero [see (20)]. In other words, the rising input power stops stimulated recombination before saturation is reached. From that point on, the input saturation power declines steadily with stronger pumping; however, the output saturation power benefits from the rising saturation gain which can cause a flat maximum in Fig. 7. Beyond that maximum, the saturation power drops sharply as the lasing threshold is approached. The dot in Fig. 7(a) represents the measurement from Fig. 6 and shows perfect agreement. The measured saturation power is close to its theoretical maximum for our current device with the maximum reflection gain being about 17 dB. Reducing the number of output mirror periods allows for more gain and higher saturation power, but the required pump current also rises (Fig. 8). For example, by reducing the top mirror reflectivity of our current device to 0.833 (six periods), we can achieve 7 dBm of output saturation power without sacrificing the 10-dB gain [see Fig. 7(a)]. However, the pump current density needs to be increased to 2.35 kA/cm^2 [see Fig. 8(a)] which is about four times higher than with our previous experiments. This pump current gives the unsaturated carrier density $N_u = 2.5 \times 10^{18}$ cm^{-3}, resulting in $g = 2200$ cm^{-1} and $G_s = 1.05$. With the 10-dB gain, the optimized device would exhibit about 420-GHz bandwidth in reflection mode (Fig. 5). This example shows how to use Figs. 5, 7, and 8 to explore design options. Large bandwidths are desirable, e.g., for multiple channels, whereas small bandwidths are needed in filter applications. For instance, selecting a smaller target bandwidth of 30-GHz in transmission mode at 10-dB gain (100-GHz gain-bandwidth product), we extract from Fig. 5 the required bottom DBR reflectivity to be about 0.982 (15 bottom
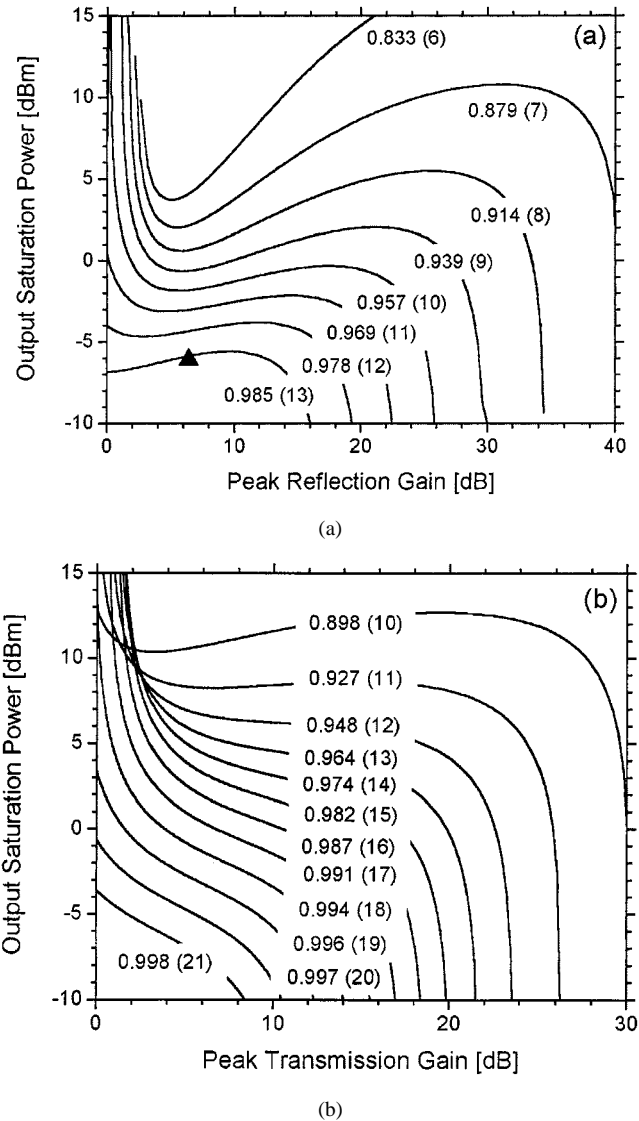

(a)

(b)

Fig. 7. Output saturation power versus peak gain for (a) reflection mode and (b) transmission mode (dot: measurement). The output mirror reflectivity (periods) is given as parameter for (a) 25 bottom mirror periods and (b) 13 top mirror periods.

periods for 13 top periods). This gives a 2-dBm saturation power [see Fig. 7(b)] and about 700 A/cm^2 required pump current density [see Fig. 8(b)].

Figs. 5, 7, and 8 allow for an easy exploration of the VCSAO design space, matching desired performance data with the required mirror reflectivity and pump current. Fig. 5 is most general and it allows for bandwidth considerations with any Fabry–Perot-type SOA. However, the curves in Figs. 7 and 8 are restricted to our 1.3-μm active region and recalculation is required for other types of active regions. Strong pumping may lead to considerable internal heating of the device which affects the quantum well gain. Higher temperature reduces and red-shifts the gain peak in Fig. 2. For any active region temperature, the appropriate function $g(N)$ can be calculated from [15]. The cavity resonance wavelength is less temperature sensitive. For strong pumping and high-temperature operation, optimized quantum wells are desirable with the room-temperature gain peak blue-shifted from the signal wavelength.
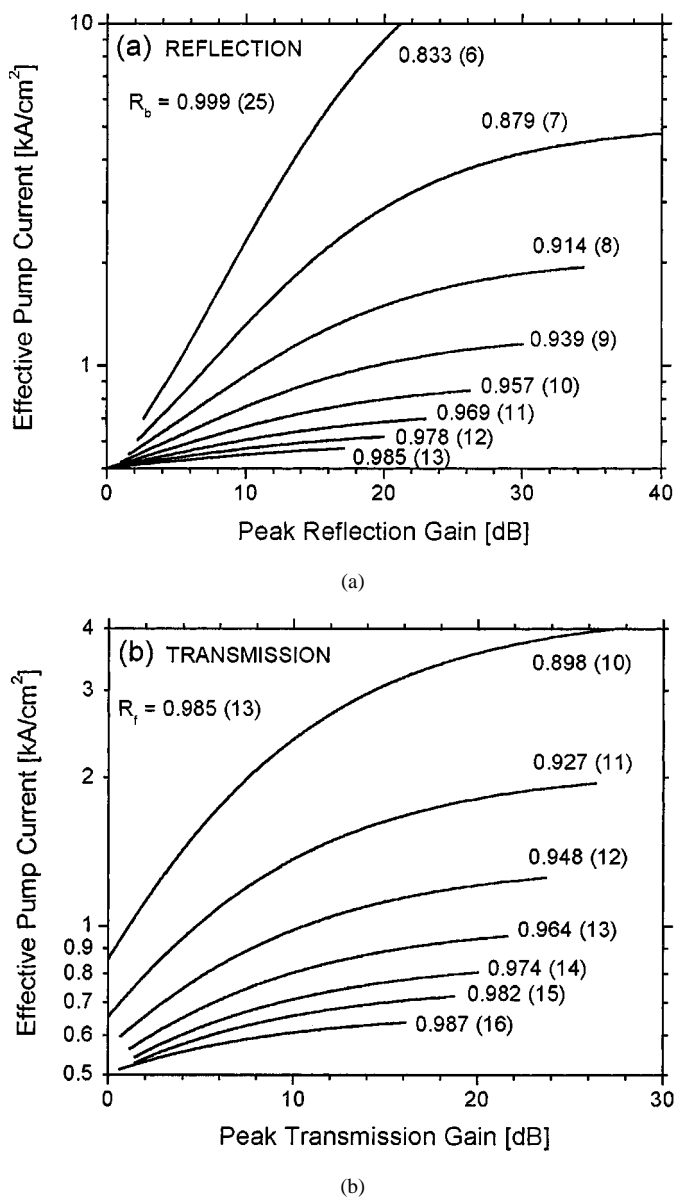
Fig. 8. Pump current densities versus peak gain corresponding to the curves in Fig. 7 for (a) reflection mode and (b) transmission mode. The bottom border indicates the present pump level.

IV. SUMMARY

We present a detailed model for gain, optical bandwidth, and saturation of vertical-cavity laser amplifiers. Distinctive features of vertical-cavity device physics are taken into account, like the penetration depth into the mirror and the standing-wave effect on the gain. Common linear approximations for gain and carrier lifetime are avoided to reliably investigate the performance at high carrier densities. Excellent agreement with measurements on novel 1.3-μm vertical-cavity amplifiers is obtained. With reduced top mirror reflectivity (six periods) and increased pumping (2.35 kA/cm^2), substantial and simultaneous improvements of optical bandwidth (420 GHz) and output saturation power (7 dBm) are predicted maintaining 10-dB reflection gain. Apart from the numerical gain calculations, the model is fully analytic and easy to apply to other types of vertical-cavity semiconductor optical amplifiers. However, more elaborate models are required to consider lateral effects.

REFERENCES

[1] D. Wiedenmann, B. Moeller, R. Michalzik, and K. J. Ebeling, "Performance characteristics of vertical-cavity semiconductor laser amplifiers," *Electron. Lett.*, vol. 32, pp. 342–343, 1996.

[2] R. Lewen, K. Streubel, A. Karlsson, and S. Rapp, "Experimental demonstration of a multifunctional long-wavelength vertical-cavity laser amplifier-detector," *IEEE Photon. Technol. Lett.*, vol. 10, pp. 1067–1069, 1998.

[3] N. Bouche, B. Corbett, R. Kuszelewicz, and R. Raj, "Vertical-cavity amplifying photonic switch at 1.5 μm," *IEEE Photon. Technol. Lett.*, vol. 8, pp. 1035–1037, 1996.

[4] S. Bjorlin, J. Piprek, B. Riou, A. Keating, P. Abraham, Y.-C. Chiu, and J. E. Bowers, "1.3-micron vertical-cavity amplifier," presented at the 25th Optical Fiber Communication Conf., Baltimore, MD, 2000.

[5] V. Jayaraman, J. C. Geske, M. H. MacDougal, F. H. Peters, T. D. Lowes, and T. T. Char, "Uniform threshold current, continuous-wave, single-mode 1300 nm vertical cavity lasers from 0 to 70°C," *Electron. Lett.*, vol. 34, pp. 1405–1407, 1998.

[6] H. Ghafouri-Shiraz, *Semiconductor Optical Amplifiers*. New York, NY: Wiley, 1995.

[7] C. Tombling, T. Saitoh, and T. Mukai, "Performance predictions for vertical-cavity semiconductor laser amplifiers," *IEEE J. Quantum Electron.*, vol. 30, pp. 2491–2499, 1994.

[8] A. Karlsson and M. Hoijer, "Analysis of a VCLAD: Vertical-cavity laser amplifier detector," *IEEE Photon. Technol. Lett.*, vol. 7, pp. 1336–1338, 1995.

[9] S. Bjorlin, B. Riou, A. Keating, P. Abraham, Y.-C. Chiu, J. Piprek, and J. E. Bowers, "1.3-micron vertical-cavity amplifier," *IEEE Photon. Technol. Lett.*, vol. 12, pp. 951–953, 2000.

[10] L. A. Coldren and S. W. Corzine, *Diode Lasers and Photonic Integrated Circuits*.   New York, NY: Wiley, 1995.

[11] S. W. Corzine, R. H. Yan, and L. A. Coldren, "A tanh substitution technique for the analysis of abrupt and graded interface multilayer dielectric stacks," *IEEE J. Quantum Electron.*, vol. 27, pp. 2086–2090, 1991.

[12] D. I. Babic, "Double-Fused long-wavelength vertical-cavity lasers," Ph.D. dissertation, Electrical and Computer Engineering Dept., Univ. California, Santa Barbara, CA, 1995.

[13] D. I. Babic and S. W. Corzine, "Analytic expressions for the reflection delay, penetration depth, and absorptance of quarter-wave dielectric mirrors," *IEEE J. Quantum Electron.*, vol. 28, pp. 514–524, 1992.

[14] S. W. Corzine, R. S. Geels, J. W. Scott, R. H. Yan, and L. A. Coldren, "Design of Fabry-Perot surface-emitting lasers with a periodic gain structure," *IEEE J. Quantum Electron.*, vol. 25, pp. 1513–1524, 1989.

[15] Z. M. Li, Photonic integrated circuit simulator in 3D (PICS3D), in XQXQXQ, Crosslight Software, Inc., Gloucester, ON, Canada, 1999.

[16] S. L. Chuang, *Physics of Optoelectronic Devices*.   New York, NY: Wiley, 1995.

[17] G. P. Agrawal and N. K. Dutta, *Semiconductor Lasers*.   New York, NY: van Nostrand Reinhold, 1993.

[18] M. J. Adams, J. V. Collins, and I. D. Henning, "Analysis of semiconductor laser optical amplifiers," *Proc. IEEE J. Optoelectronics*, vol. 132, pp. 58–63, 1985.

Joachim Piprek (SM'98) received the Ph.D. degree in solid state physics from Humboldt University, Berlin, Germany, in 1986.

He has worked in industry and academia on the design and analysis of optoelectronic devices. He is currently an Adjunct Associate Professor with the University of California at Santa Barbara. His research interests include in-plane and vertical-cavity lasers, novel semiconductor materials, and advanced computer simulation.

Staffan Björlin received the M.S. degree in engineering physics from the Royal Institute of Technology, Stockholm, Sweden, in 2000. He is currently working toward the Ph.D. degree in electrical engineering at University of California at Santa Barbara.

His research interests include design and characterization of vertical-cavity semiconductor optical amplifiers and vertical-cavity lasers.

John E. Bowers (F'93) received the Ph.D. degree in applied physics from Stanford University, Stanford, CA, in 1981.

He was with Honeywell and AT&T Bell Laboratories before joining University of California at Santa Barbara in 1987, where he is currently a Professor of Electrical Engineering, the Director of the Multidisciplinary Optical Switching Technology Center (MOST), and Member of the Heterogeneous Optoelectronics Technology Center (HOTC) and the NSF Center on Quantized Electronic Structures (QUEST). His main research interests include the development of novel optoelectronic devices for the next generation of optical networks.